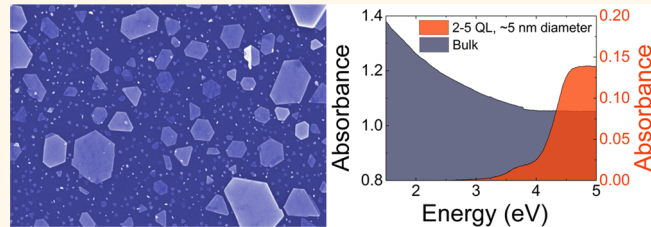


The Changing Colors of a Quantum-Confining Topological Insulator

Anthony Vargas, Susmita Basak, Fangze Liu, Baokai Wang, Eugen Panaitescu, Hsin Lin, Robert Markiewicz, Arun Bansil, and Swastik Kar*

Department of Physics, Northeastern University, Boston Massachusetts, United States

ABSTRACT Bismuth selenide (Bi_2Se_3) is a 3D topological insulator, its strong spin–orbit coupling resulting in the well-known topologically protected coexistence of gapless metallic surface states and semiconducting bulk states with a band gap, $E_g \simeq 300$ meV. A fundamental question of considerable importance is how the electronic properties of this material evolve under nanoscale confinement. We report on catalyst-free, high-quality single-crystalline Bi_2Se_3 with controlled lateral sizes and layer thicknesses that could be tailored down to a few nanometers and a few quintuple layers (QLs), respectively. Energy-resolved photoabsorption spectroscopy ($1.5 \text{ eV} < E_{\text{photon}} < 6 \text{ eV}$) of these samples reveals a dramatic evolution of the photon absorption spectra as a function of size, transitioning from a featureless metal-like spectrum in the bulk (corresponding to a visually gray color), to one with a remarkably large band gap ($E_g \geq 2.5 \text{ eV}$) and a spectral shape that correspond to orange-red colorations in the smallest samples, similar to those seen in semiconductor nanostructures. We analyze this colorful transition using *ab initio* density functional theory and tight-binding calculations which corroborate our experimental findings and further suggest that while purely 2D sheets of few QL-thick Bi_2Se_3 do exhibit small band gaps that are consistent with previous ARPES results, the presently observed large gaps of a few electronvolts can only result from a combined effect of confinement in all three directions.



KEYWORDS: topological insulator · bismuth selenide · band gap · chemical vapor deposition · quantum dots

Since the earliest demonstration that the bulk $\text{Bi}_{1-x}\text{Sb}_x$ system can sustain massive Dirac particles in a quantum spin-Hall phase while simultaneously preserving topologically protected gapless Dirac-like surface states,¹ 3D topological insulators (TIs)^{2–6} have become one of the most exciting research topics in condensed matter physics. The gapless (metal-like) surface states feature elementary excitations in a spin-momentum locked configuration on the Dirac cones with energies that lie within the bulk band gap, and these quantum states are thought to be robustly protected even in the presence of nonmagnetic scatterers,^{6,7} although there is some evidence indicating the limits of this hypothesis.^{8,9} This represents the first 3D analogy of a type of time-reversal symmetry that was previously observed only in 2D systems such as edge states of quantum-Hall¹⁰ or quantum spin-Hall systems.^{11–13} The surface states of 3D TIs have been proposed to be a potential breeding ground for exotic particles such as Majorana fermions¹⁴ and magnetic monopoles,¹⁵ and the topological protection is potentially

attractive for dissipation-free information processing⁵ and fault-tolerant quantum computation applications.¹⁶

The possibility of exploring and exploiting these and other novel phenomena has spurred the development of a variety of 3D TI systems. A textbook example of this is bismuth selenide (Bi_2Se_3), a TI with a single Dirac cone surface state which is energetically positioned in the bulk band gap of $E_g \simeq 300$ meV.^{6,17–19} Its TI properties were predicted⁶ and subsequently experimentally verified¹⁷ at room temperature. Along with Bi_2Se_3 , Bi_2Te_3 and Sb_2Te_3 have also received a lot of recent attention, as a number of different fabrication methods have allowed high-quality crystals to be investigated through ARPES, STM, and field-modulated and temperature dependent transport.^{19–23} In particular, owing to the layered nature of these materials, easy-to-fabricate approaches such as micro-mechanical exfoliation^{23–25} and chemical vapor deposition^{22,26,27} have complemented the more conventional molecular beam epitaxy techniques,^{20,21,28–30} opening up

* Address correspondence to s.kar@neu.edu.

Received for review August 1, 2013 and accepted January 15, 2014.

Published online January 15, 2014
10.1021/nn404013d

© 2014 American Chemical Society

an array of experiments accessible to a wide variety of research disciplines.

One area that has been receiving rapidly growing interest is exploring the effect of confinement in these novel materials, both mechanical confinement in ultra-thin 2D films (down to a few quintuple layers or QLs) and electronic confinements, such as those originating from band bending at the surface of Bi_2Se_3 ³¹ that results in strong spin–orbit splitting of the quantum-confined states in the conduction band.³² Much work has been invested in thin films and nanostructures of Bi_2Se_3 with enhanced surface-to-volume ratios in an attempt to reduce the bulk contribution and allow greater access toward probing the exotic surface states. For example, thin films have been grown using molecular beam epitaxy (MBE),^{20,21,28–30} nanoplates *via* chemical^{33–35} and mechanical exfoliation methods,^{23–25} and a variety of nanostructures, including nanowires, nanoribbons, and nanoplates^{22,26,27} have been produced using chemical vapor deposition (CVD) methods. In this context, a fundamental question of extreme importance is how the electronic properties of this system evolve with increased quantum confinement, especially at the few QL-level. Previous works have reported QL-dependent studies in 2D/thin film architectures of Bi_2Se_3 including Raman shifts,^{25,33} transport properties,²⁸ and the appearance of a surface state band gap.^{19–21,28} As the sample thickness begins to approach the penetration depth³⁶ of the surface states, $l = \hbar v_F/E_g$ (~ 1.5 nm for Bi_2Se_3), these states begin to interact with each other through quantum tunneling. A number of recent ARPES experiments have shown a clear evidence of gap-opening in the surface states in samples below 5QL thickness,^{20,21} that coexists with bulk band-gaps (E_g) of a few hundred millielectronvolts,^{21,23} though 2D films of 2–3 QL thickness still retain their spin-polarized bands. However, it appears that there has been no systematic study of samples that approach a true confinement in all three directions, *i.e.*, 0D samples.

In this work, we investigate the evolution of the electronic properties of Bi_2Se_3 as a function of sample size approaching a few nanometers in all dimensions, using energy-resolved photoabsorption spectroscopy. Going beyond past investigations that looked at ultra-thin (2D) samples, we explore the possibility of opening a larger band gap within the few-QL regime using quantum confinement effects in the other 2 dimensions. Samples of different lateral sizes and thicknesses were stoichiometrically grown in a catalyst-free environment on silicon dioxide wafers with no epitaxial relation to the growth substrate. Measurements were performed on crystals suspended in a pure DI water suspension rather than on a substrate. We believe that in this manner, we were able to obtain the intrinsic properties of these crystals without any effect of substrate-induced strain, doping, band-bending, *etc.*, that

TABLE 1. A Summary of Growth Conditions for the Samples Described in This Paper Detailing the Location of the Receiving SiO_2/Si Substrates with Relation to the Center of the CVD Furnace, CVD Chamber Temperature, and Growth Time

sample	distance from center (cm)	temperature (°C)	time (min)
S1	15	450	1
S2	14	500	1
S3	15	500	10
S4	13	500	1

naturally result from MBE-growth or inadvertent contamination/doping effects due to lithography/metallization that occur in samples prepared for transport measurements. We note that due to the small size of these crystals, ARPES or conventional transport measurements would be quite difficult to perform. We find that the photon-energy dependence of absorbance changes significantly from bulk all the way down to a few QLs. Most importantly, we find that nanoflakes of 2–6 QL Bi_2Se_3 with an average lateral size ~ 7 nm show a large band gap $2 \text{ eV} < E_g < 2.6 \text{ eV}$, which is 3–5 times the band gap reported for thin films of similar thicknesses. Hence, this 0D confinement could potentially lead to exciting new physics beyond those being currently explored in ultrathin films of topological insulators.^{20,21} The obtained results were verified by suspending the nanoflakes in other liquid media such as isopropanol, and no significant difference was observed, implying that the surrounding medium played little or no role in this large gap-opening. Nearly identical results were obtained from samples that were directly exfoliated from bulk Bi_2Se_3 by ultrasonication and nanopore filtration, providing further confirmation that the gap-opening was not an artifact of contamination in the growth-process. We present systematic studies of optical absorption for $1.5 \text{ eV} < E_{\text{ph}} < 6 \text{ eV}$ in Bi_2Se_3 samples from the bulk to the few-QL limit. Since we did not have an integrating sphere in our measurement setup, effects of scattering could not be separately estimated in the energy-dependence of the photon absorption, A . However, this does not affect our main results which focus on the absorption edge E_g below which $A = 0$, *i.e.*, the photon energy below which there was 100% transmittance, with no measurable scattering effects.

SAMPLE GROWTH AND CHARACTERIZATION

Synthesis of the Bi_2Se_3 nanoplatelets was done *via* catalyst-free chemical vapor deposition (CVD).^{22,26,27} It was found that the dimensions and shape of the single-crystal nanoplatelets depended most sensitively on the CVD furnace temperature as well as growth time and the position of the receiving substrate from the center of the CVD chamber. Suitable growth conditions (see Table 1) were developed to obtain samples with both narrow as well as broadly distributed sizes and

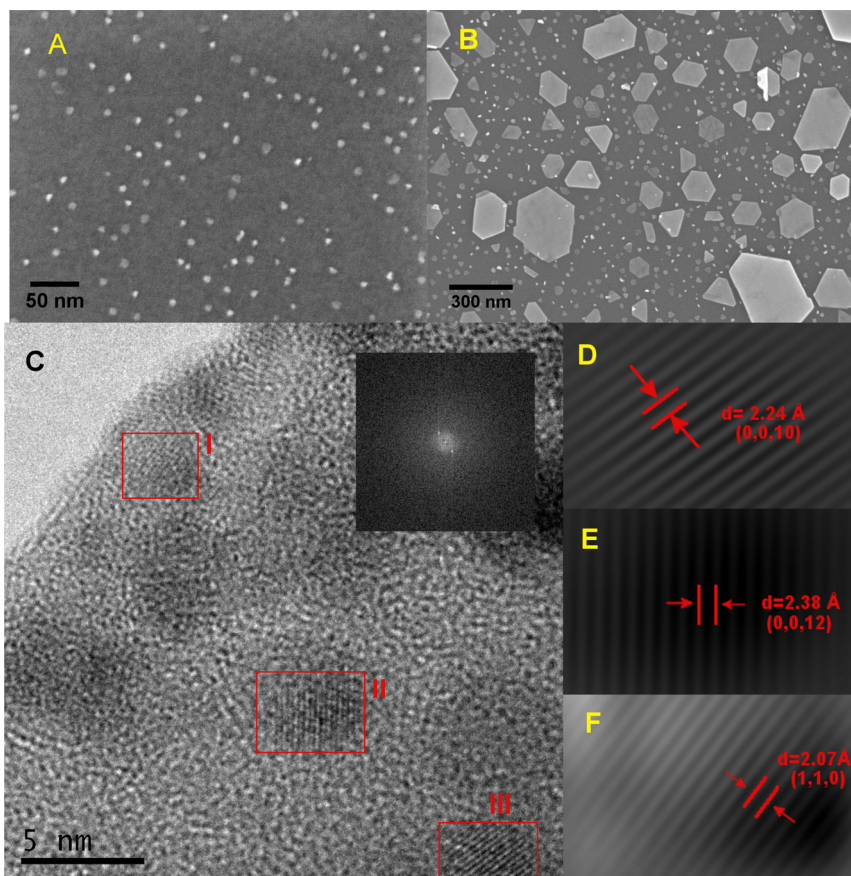


Figure 1. Typical SEM images of (A) sample S1 and (B) sample S3. (C) A typical TEM image of sample S1. Inset is an example FFT of area I. (D–F) Inverse transforms of contrast-enhanced FFTs of the marked areas of 1C, shown from top to bottom. These digitally enhanced images were used to obtain the lattice fringes as shown.

thicknesses. The end products were characterized using scanning electron microscopy (SEM), tunneling electron microscopy (TEM), energy-dispersive X-ray spectroscopy (EDX), Raman spectroscopy, and X-ray diffraction (XRD). A large number of samples were fabricated and characterized, and in this paper, we report on four well-characterized samples (as shown in Table 1) that are representative of the various size/thickness ranges of samples on which measurements were performed.

Figures 1A,B show typical SEM images of CVD grown Bi_2Se_3 nanoplatelets from 2 different sets of growth conditions. We found that samples larger than a few nanometers in size preferred to form nanoplatelets with trigonal or hexagonal morphologies and grow flat on the surface. TEM analysis was conducted on sample S1, which had the smallest Bi_2Se_3 crystals. The nanoplatelets were released by ultrasonication from their growth substrate into deionized water, and this suspension was drop cast onto a holey carbon TEM grid. Figure 1C is a representative TEM image of the smallest Bi_2Se_3 nanocrystals (sample S1) which ranged from 3 to 5 nm in size, clumped together in random orientations. These sizes agree extremely well with those obtained from SEM measurements performed on the parent substrate (see later). To measure the crystal-plane

spacings, the nanocrystal fringes (as shown by red boxes I, II, and III in Figure 1C) in the TEM images were digitally processed using a 2D Fourier transform scheme, contrast enhanced (see inset, Figure 1C), and inverse transformed to obtain the 2D Fourier-transform filtered lattice fringes (Figures 1D–F). The nanocrystals were found to have plane spacings consistent with various crystal orientations of Bi_2Se_3 (Figures 1D–F), indicating that our CVD process was indeed producing Bi_2Se_3 for the smallest samples.

For larger samples, we performed EDX measurements which gave the expected ratio of 2 bismuth to 3 selenium, as shown in Figure 2A. XRD measurements show that the nanoplatelets grow almost entirely in the (001) hexagonal direction (Figure 2B). There are traces of (107) and (015) growth directions and these may arise from the deviations occurring at the contact of two separate nanoplatelets during the growth process. Raman analysis of the Bi_2Se_3 nanoplatelets showed the expected Raman shifts of 131 and 174 cm^{-1} (Figure 2C).³³ Bi_2Se_3 also possesses an additional Raman peak at 72 cm^{-1} which was undetectable in our system since it was below the cutoff filter on our Raman spectrometer. According to previous works, which report a shifting of the Raman peaks in samples with

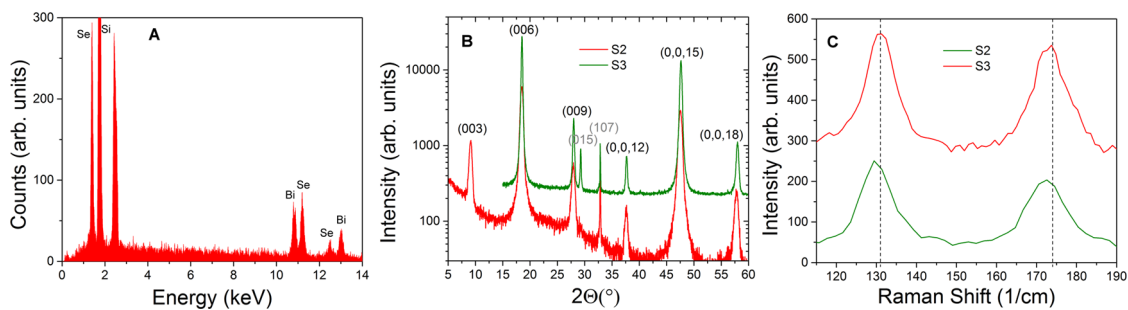


Figure 2. (A) Typical EDX measurement of Bi_2Se_3 nanoplatelets. (B) XRD data showing majority of grown nanoplatelets with a preferred (001) hexagonal direction. (C) Raman data with dashed lines indicating expected Raman shifts of 131 and 174 cm^{-1} for bulk Bi_2Se_3 .

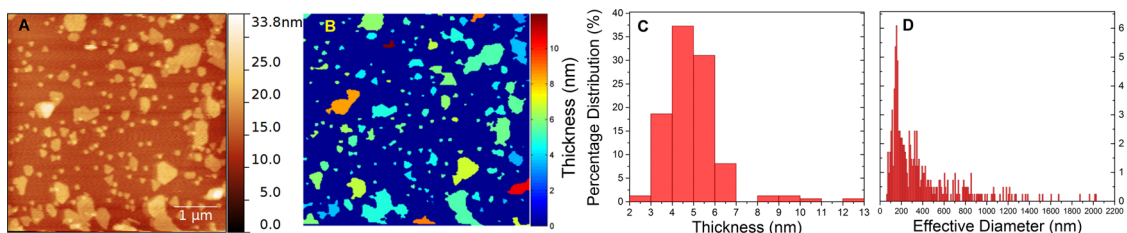


Figure 3. (A) AFM of typical as-grown sample of Bi_2Se_3 on Si. (B) Height map of shown AFM image. (C) Thickness distribution of shown AFM image. (D) Effective lateral diameter distribution of shown AFM image.

few QLs, our Raman peaks for S2 and S3 correspond to an expected thickness of $\sim 8\text{ nm}$ for S2 and $\sim 16\text{ nm}$ for S3, which also match remarkably well with the median sizes obtained in AFM measurements.³³

The thickness of the nanoplatelets was measured using atomic force microscopy (AFM). Figure 3A shows an AFM image of S2 with a distribution of different thicknesses and lateral diameters. This is typical of our CVD grown samples. With the use of a collection of AFM images from the various samples and custom Matlab code, which automatically detected nanoplatelets from the AFM topographical data and calculated the average *c*-axis thickness of each nanoplatelet (Figure 3B), thickness distributions were obtained (Figure 3A's thickness distribution shown in Figure 3C) along with the effective diameter (the diameter of a circle of equivalent area) distributions (Figure 3A's effective diameter distribution shown in Figure 3D). For sample S1 (Figure 1A), in which the effective diameters of the flakes were mostly smaller than the tip radius of our AFM, we used the SEM image of Figure 1A to obtain the diameter distribution. The trend was found that longer growth times, higher growth temperatures, and shorter distances from the furnace center gives rise to larger thicknesses and lateral sizes.

RESULTS AND DISCUSSION

Photon absorption experiments were performed on the Bi_2Se_3 nanoplatelets after they were released from their parent substrate into deionized water using a low-power bath-type ultrasonicator. After the sonication process, inspection of the parent substrates *via* SEM

showed that nearly all the nanoplatelets went into the aqueous suspension. A suspension containing “bulk” Bi_2Se_3 was separately obtained by ultrasonication of pure, commercial Bi_2Se_3 pieces and collecting the residue after filtering through a membrane filter (Millipore) with $10\text{ }\mu\text{m}$ pore size. The filtration was performed in a commercially purchased standard vacuum filter setup with an all-glass vacuum filter holder. The Bi_2Se_3 dispersions were then analyzed using UV-vis photoabsorption spectroscopy. Figure 4A shows the photoabsorbance spectra of aqueous suspensions of nanoplatelet samples S1–S4 and the “bulk” Bi_2Se_3 sample, corrected for the background absorption spectrum of water and the quartz cuvette. The thickness and effective diameter distributions for each sample are shown in Figures 4B,C, respectively. The distributions show a peak for S1 and S2 around $3\text{--}4\text{ nm}$ thickness and lateral effective diameters of 7 and 16 nm , respectively, with the diameter distribution of S1 being much narrower (*i.e.*, these samples were much more monodispersed) compared to that of S2. The larger samples, S3 and S4, have much broader distributions. It was found that the photoabsorbance of Bi_2Se_3 changes significantly as the thickness approaches a few QLs, and the effective diameter decreases. We see from Figure 4A that bulk-sized Bi_2Se_3 pieces have a featureless photoabsorbance that decreases very slowly with increasing photon energy. The large, nearly homogeneous absorption with a slightly higher spectral weight in the low-energy regime is expected to give samples a gray color which matches with the visual inspection of as-received bulk samples.

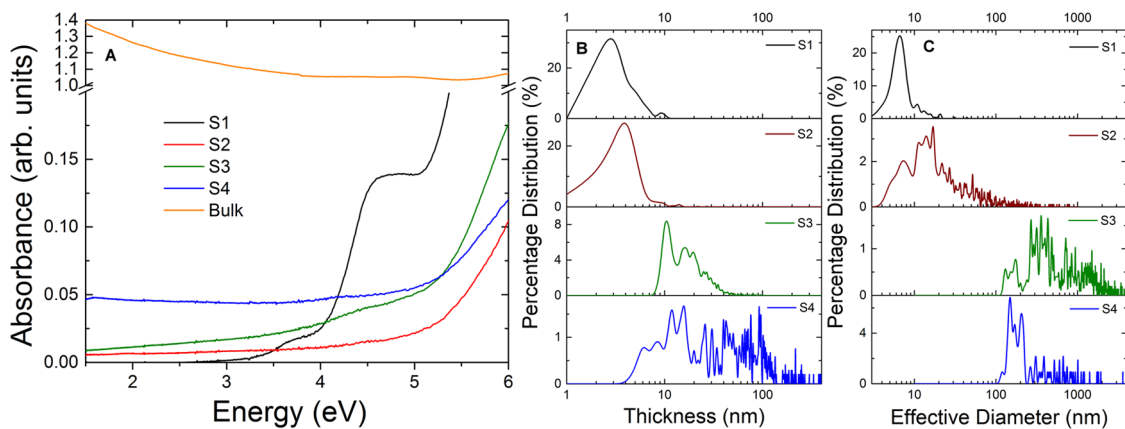


Figure 4. (A) Energy-resolved photoabsorbance spectra of bulk and nanoscale Bi_2Se_3 samples of various thicknesses and lateral sizes. (B) The thickness distribution and (C) effective lateral diameter distribution of the samples shown in (A), obtained by AFM/SEM image analysis, as described in the text.

As the thickness approaches a few QLs and effective diameter decreases, the energy dependence flattens and begins to invert so that more high-energy photons are absorbed than low-energy ones. The trend reaches a dramatic transformation in the smallest samples, where no photons are absorbed over a band of energies all the way up to the blue region of the visible spectrum, and the remaining portion of the spectrum corresponds to an orange-red coloration in the smallest samples.

To ascertain that the large band gap observed in extremely small samples of Bi_2Se_3 is not a result of accidental contamination during the CVD synthesis process, a number of samples were prepared using a “top-down” approach whereby aqueous suspensions of commercially purchased Bi_2Se_3 powders were subjected to long-term ultrasonication processes which resulted in suspended particles that ranged from micrometers to nanometers in size. These samples were then sequentially vacuum-filtered through commercially purchased cellulose filters of decreasing pore size: $10\ \mu\text{m}$, $1.2\ \mu\text{m}$, $100\ \text{nm}$, and $25\ \text{nm}$. The photoabsorbance measurements were repeated on these suspensions between each filtering step. Figure 5A reveals the photoabsorbance spectra of these samples. We see that each curve has a flat, featureless low-energy absorbance spectrum with a clear set of features in the high-energy region. With decreasing size-distribution, the low-energy, flat portion of the spectrum decreased almost completely, indicating that the larger pieces of samples were responsible for this region of the photoabsorbance spectrum. Significantly, the high-energy portion of the spectrum maintains strong features all the way to the sample with the smallest size-scales ($d \leq 25\ \text{nm}$). Figure 5B is a magnified view of absorbance vs energy data of sample S1 and the $25\ \text{nm}$ filtered sample ultrasonicated from bulk (from Figure 4A and Figure 5A, respectively) which confirms that the absorbance reaches $A = 0$ at $E_g \sim 2.5\ \text{eV}$ for the smallest sample S1, implying that an optical band gap of $\sim 2.5\ \text{eV}$ opens up when Bi_2Se_3 nanoslatelets reach a quantum confinement of a few QLs in thickness

and a few nanometers in effective diameter. The $25\ \text{nm}$ filtered pieces of Bi_2Se_3 contain a relatively broader thickness-distribution ($\leq 25\ \text{nm}$) compared to sample S1 ($\leq 7\ \text{nm}$). As a result, when magnified 100 times, there was a very small but finite absorbance at low energies that prevented us from estimating the absorption-edge of the smaller particles within the distribution of sizes. Unfortunately, we could not obtain filters with smaller pore-sizes to match the two size-distributions (*i.e.*, that of fabrication by CVD vs ultrasonication). However, we note that despite the completely different fabrication approaches, and except for a small baseline difference in absorbance at the lowest energy values (Figure 5B), the absorption curve-shapes (as a function of energy) are strikingly similar even at the highest magnification level. We believe that the evolution of the absorbance curves as a function of size-distribution in Figure 5A gives clear indication that a band gap would be seen in these samples if further smaller size-distributions could be achieved *via* filtration through pores $\ll 25\ \text{nm}$. These experiments (using both CVD and mechanically exfoliated samples) were also verified in other dispersion media (*e.g.*, 2-propanol), resulting in identical appearance of a band gap in the smallest samples, establishing that the observed evolution of the absorption spectra (color) or the appearance of a band gap in Bi_2Se_3 is not an artifact of synthesis or the surrounding media.

The observed metal-to-insulator transition of the surface states at few QLs was previously theoretically predicted^{36,37} and also experimentally explored.^{20,21} However, both predictions and measurements assumed samples of planar geometry that were subjected to 2D confinement, wherein band gaps of a few hundred meV were predicted, and also confirmed in large area thin films of Bi_2Se_3 . It appears that the potential impact of complete confinement in all three dimensions has not been explored. Since Bi_2Se_3 is a direct band gap material, the rather large band gap of $E_g \sim 2.5\ \text{eV}$ places the smallest Bi_2Se_3 in a region of high technological importance, namely low-cost solar

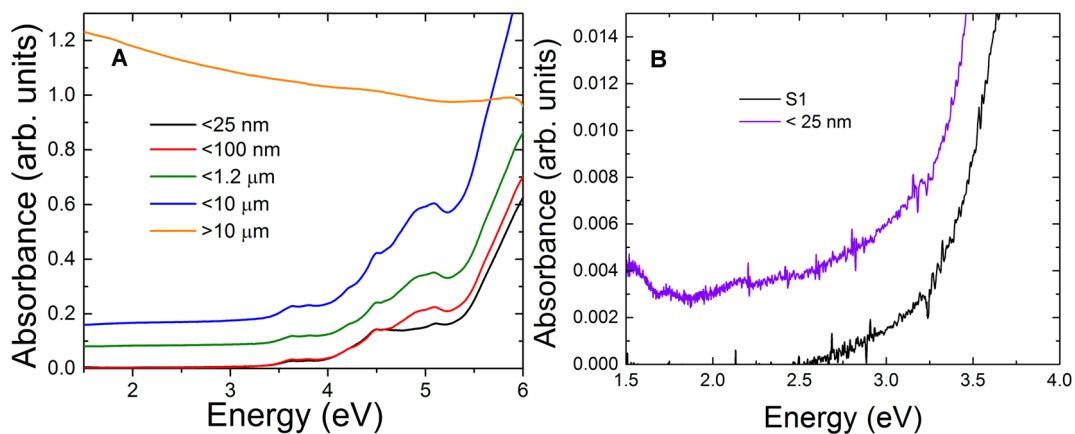


Figure 5. (A) Photoabsorbance spectra of Bi₂Se₃ samples of different size-distributions obtained by ultrasonication of a commercially obtained bulk sample that was filtered through membranes of progressively smaller sizes. (B) Zoomed view of the photoabsorption spectrum of sample S1 showing the optical absorbance reaching 0 at ~ 2.5 eV. In this highly magnified scale, the absorbance curve of the ultrasonicated samples filtered through 25 nm pores retain a very small, featureless residual absorbance consistent with their larger size-range compared to sample S1.

cells, photodetectors and display devices. A matter of significant importance is how far the quantum confinement in all three dimensions is critical for these large band gaps, and whether size-control can be an effective approach for tuning the electronic properties in a continuous manner. To understand this, and get a better insight on the experimental observations, we carried out a systematic study of the size-effects of Bi₂Se₃ using the first-principles method as well as tight-binding model calculations. The optical absorption coefficient which is a measure of how far light with a specific energy can penetrate the sample is given by

$$\alpha(\omega) = \sqrt{2}\omega[(\varepsilon_1^2(\omega) + \varepsilon_2^2(\omega))^{1/2} - \varepsilon_1(\omega)]^{1/2} \quad (1)$$

where ε_1 and ε_2 are the real and imaginary parts of the frequency (ω) dependent dielectric function, respectively. Direct interband transitions contribute to the imaginary part and hence $\varepsilon_2(\omega)$ is determined by summing all possible vertical transitions from the occupied to unoccupied states. Within the notation of projector-augmented wave (PAW) methodology,³⁸

$$\begin{aligned} \varepsilon_2^{\alpha\beta}(\omega) = & \frac{4\pi^2 e^2}{\Omega} \lim_{q \rightarrow 0} \frac{1}{q^2} \sum_{c, v, \mathbf{k}} 2w_{\mathbf{k}} \delta(\varepsilon_{c\mathbf{k}} - \varepsilon_{v\mathbf{k}} - \omega) \\ & \times \langle u_{c\mathbf{k} + e_{\alpha}\mathbf{q}} | u_{v\mathbf{k}} \rangle \langle u_{c\mathbf{k} + e_{\beta}\mathbf{q}} | u_{v\mathbf{k}} \rangle^* \end{aligned} \quad (2)$$

where the indices c and v refer to conduction and valence band states respectively, $u_{c\mathbf{k}}$ is the cell periodic part of the orbital at the \mathbf{k} -point k and $w_{\mathbf{k}}$ is the \mathbf{k} -point weight. The real part ε_1 is obtained by the usual Kramers–Kronig transformation

$$\varepsilon_1^{\alpha\beta}(\omega) = 1 + \frac{2}{\pi} P \int_0^\infty \frac{\varepsilon_2^{\alpha\beta}(\omega')\omega'}{\omega'^2 - \omega^2} d\omega' \quad (3)$$

where P denotes the principal value of the integral. The optical properties are calculated within the density functional theory, based on the generalized gradient

approximation (GGA)³⁹ using the full-potential projected augmented wave method^{40,41} as implemented in the VASP package.^{40,41} The 1QL, 2QL and 3QL slab models with a vacuum thickness larger than 10 Å are used in this work. The electronic structure calculations were performed over $11 \times 11 \times 1$ Monkhorst-Pack k-mesh with the spin–orbit coupling included self-consistently. Atomic positions are taken from the experimental bulk structure.

Near the band edge, the absorbance α is expected to scale as $(\alpha h\nu)^{1/\eta} \sim (h\nu - E_g)$, where E_g is the optical band gap.⁴⁵ A plot of $(\alpha h\nu)^{1/\eta}$ as function of photon energy $h\nu$ is usually called a Tauc plot, where $\eta = 1/2, 3/2, 2$, or 3 for direct allowed transitions, direct forbidden transitions, indirect allowed transitions, and indirect forbidden transitions, respectively. While Bi₂Se₃ has been described as on the verge of being indirect,⁴⁶ the theoretical gap seems to remain direct as a function of film thickness. Hence, we assume Bi₂Se₃ is direct gap, in which case $\eta = 0.5$. Figure 6 compares the thickness dependence of the Tauc plots of Bi₂Se₃ between experiment (panel A) and theory (panel B). The theoretical spectra are calculated for two-dimensional (2D) infinite sheets of various thicknesses ranging from 1 to 3 quintuple layers (QLs) (black, red, and green curves, respectively) and for the bulk Bi₂Se₃ (orange curve). One can see that there is distinct correlation in the shapes and evolution of the theoretical and experimental Tauc plots as a function of sample size. In both cases, there is a clear trend of lowering of the low-energy spectral weight with decreasing sample size resulting in the clear opening of a band gap in the smallest samples. However, it is also clear that the theoretical optical gap for the smallest thickness (1 QL) is much smaller than the corresponding observed experimental gap. These observations indicate that modeling the smallest samples (with a peak lateral size ~ 7 nm) as 2D planar (infinite) sheets with finite layer thickness is not sufficient to explain the large observed gap, and we need

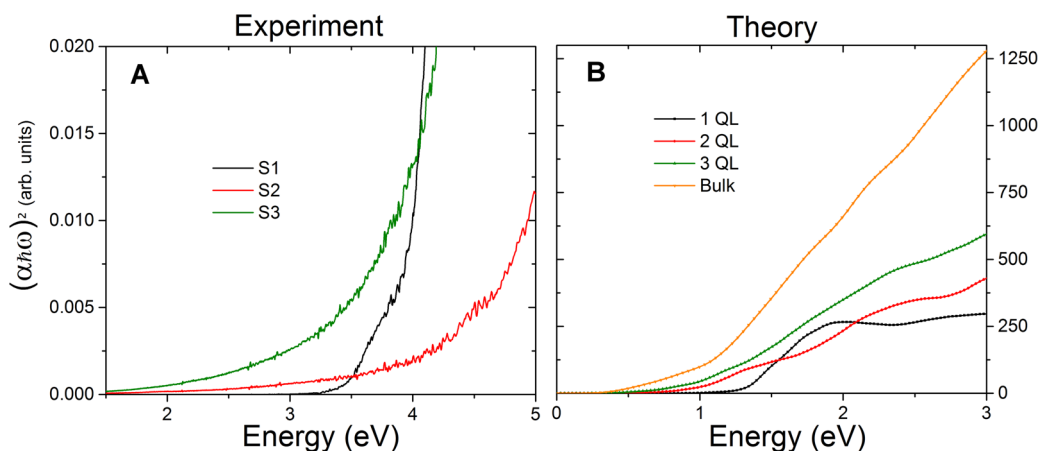


Figure 6. Tauc plot of optical absorbance as function of thickness of the nanoplatelets. (A) Experiment, (B) first-principles calculations for slabs of thicknesses 1–3 QL (black, red, and green, respectively) and bulk (orange).

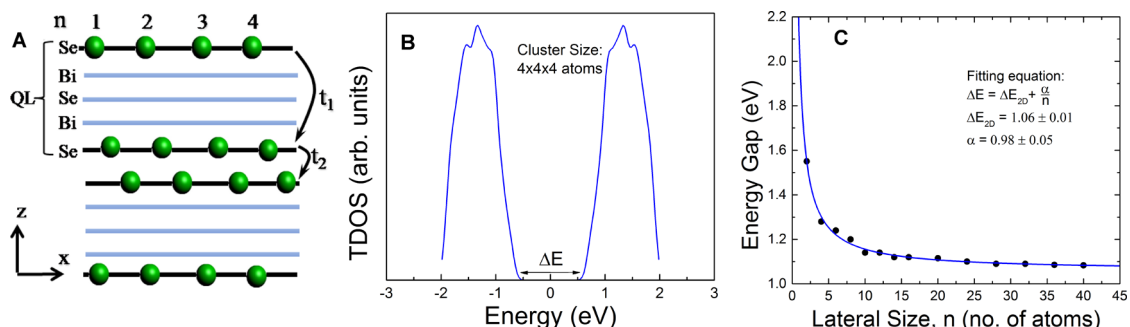


Figure 7. (A) Schematics of the $x-z$ plane of a $4 \times 4 \times 4$ atom cluster of Bi_2Se_3 . (B) Total density of states for the same cluster. (C) Gap-size as a function of the lateral size (n atoms) of clusters with a fixed 2 QL (4 atoms) thickness.

to invoke three-dimensional (3D) confinement in our modeling, *i.e.*, treat the smallest samples as 0D crystals.

To understand the effect of 3D confinement, we carried out model calculations for small Bi_2Se_3 crystallites based on tight-binding theory. We note that even the smallest-sized crystallite has a large number of atoms and performing first-principles calculations on such a system is computationally quite expensive. We constructed a two-orbital tight-binding (TB) model in the rhombohedral lattice where each QL was represented by two p_z orbitals associated with two equivalent Se atoms in one unit cell, as shown in Figure 7A.⁴⁷ The tight-binding Hamiltonian, by construction, captures the essential features of the band structure near the Γ point. Within this model a small crystallite can be viewed as a cluster of atoms with a shape of a rectangular parallelopiped with z -axis being equivalent to the (111) direction of the rhombohedral lattice. The $x-z$ plane of a 64 Se-atom cluster ($4 \times 4 \times 4$) is shown schematically in Figure 7A. We considered the nearest neighbor hoppings along x - and y -directions within a Se-layer and hopping along z -direction between the two equivalent Se layers within a QL (t_1) and between the two adjacent Se layers in the neighboring QLs (t_2). The spin–orbit coupling was incorporated in terms of an intra-Se-layer hopping. Note that this model has no dangling bonds and it possesses a symmetrical

shape, and we find that it captures the slab thickness dependence of the gap in reasonable accordance with first principle results. However, even for 0D samples the gap does not reach the large size seen experimentally for the bulk hopping parameters. We find that we can reproduce the largest observed gap size if the interlayer hopping t_1 changes from -1 to -1.55 eV, suggestive of a small change in layer spacing. In Figure 7 we use an average $t_1 = -1.25$ eV. The total density of states (TDOS) for a 64 Se-atom cluster ($4 \times 4 \times 4$) is presented in Figure 7B which shows a large gap (ΔE) of the order of 1.28 eV, while the gap for the smallest cluster of size ($2 \times 2 \times 4$) is closer to 1.55 eV, which is much larger than the gap seen in the 2D sheets, and is encouragingly closer to that seen experimentally in the smallest samples. Further, this gap is found to decrease for samples with laterally larger cluster sizes. In Figure 7C, we analyze the variation of the gap-size as a function of the lateral size (n atoms) with a fixed thickness (4 atoms or 2 QLs along z -direction), *i.e.*, these clusters have $2 \times 2 \times 4$ Se atoms, $3 \times 3 \times 4$ Se atoms, and so on. Initially, the gap-size decreases rapidly with the lateral size, but eventually it becomes a slowly varying function. The asymptotic value of ΔE (or ΔE_{2D} , estimated by fitting the data with an empirical curve $\Delta E = \Delta E_{2D} + \alpha/n$) approaches 1.1 eV which is close to the optical gap observed for 2D infinite sheet of 2 QL thickness as shown

in Figure 6B by the red dotted curve. As the crystal size decreases, the gap grows in a manner which is nearly inversely proportional to the lateral size. Notably, a similar behavior is predicted, for example, in PbS quantum dots where the gap also scales inversely with the dot radius.⁴⁸ Although quantum confinement effects are at play in both materials, we should keep in mind that Bi₂Se₃ is a layered material with strong intraplane interactions and a weaker interplane coupling, while PbS is a 3D cubic lattice with no obvious 2D symmetry. The size dependence of the bandgap in Bi₂Se₃ is thus intrinsically more complex and involves the interplay of in-plane and out-of-the-plane confinement effects.

CONCLUSION

We have established, using a combination of experimental and theoretical investigations, the dramatic manner in which the electronic properties of a known topological insulator, *i.e.*, Bi₂Se₃, evolve as a function of thickness (down to 1QL 2D confinement) and lateral size (down to a few nanometers). We note that although the pathways for reaching 0D confinement from bulk size-scales are different for the experimental and theoretical approaches, their end-results at the

smallest size-scales have quite good quantitative agreement. The visual analogy of the photoabsorption spectra of the samples of different sizes is a color transition as a function of quantum confinement in this system. The resulting samples at the smallest size-scales have band gap values that are of the order of electronvolts, which is larger than that of similar-sized quantum dots of PbS and PbSe,⁴⁹ but similar to that of CdS quantum dots of comparable dimensions. It is well-known that these sulphides and selenides are highly attractive for a number of optoelectronic applications such as multiple exciton generation (MEG)-based solar cells,⁴⁹ high-quantum gain photodetectors,⁵⁰ and light emitters.⁵¹ In this context, it would be quite interesting to explore the interaction of polarized photons⁵² with carriers in these novel confined states, as well as pursue investigations of related photoemission processes. Hence, the controlled development of this and other TI nanosystems could open new frontiers of nanoelectronics and optoelectronics, resulting in potential room-temperature applications of these materials, beyond spintronics and quantum computation.

METHODS

Bi₂Se₃ nanoplatelets were grown *via* catalyst-free chemical vapor deposition (CVD)^{22,26,27} in a horizontal tube furnace (Lindberg/Blue M). Source material of 0.1g Bi₂Se₃ powder (99.999%, Alfa Aesar) was placed in the hot center of the furnace with Si wafers (N-doped, (100)) placed 11–16 cm downstream. After the system was pumped down to a base pressure of about 20 mTorr, a 30 sccm Ar flow was introduced which gave a final growth pressure of about 360 mTorr. The center of the furnace was then heated to a temperature of 450–500 °C which gave a substrate temperature of 350–450 °C depending on center temperature and substrate distance from the center. The furnace was held at this temperature for 1–10 min and then allowed to cool in the furnace. SEM images were taken with a Hitachi S-4800. TEM images were taken with a JEOL 2010F. XRD and Raman measurements were done with a Philips X-ray diffractometer and Remishaw Ramascope (using a 488 nm laser), respectively. AFM measurements were done with Nanomagnetics Instruments Ambient AFM and Park Systems XE150 AFM. Samples were sonicated from their growth substrates into a DI water solution using a bath-type sonicator. UV–vis photoabsorption spectroscopy was performed using a Perkin-Elmer Lambda 35.

Conflict of Interest: The authors declare no competing financial interest.

Acknowledgment. The experimental part of this work was partially supported by an NSF Award: ECCS-1351424, and a Northeastern University Provost's Interdisciplinary seed grant. The theoretical work is supported by the US Department of Energy, Office of Science, Basic Energy Sciences contract number DE-FG02-07ER46352, and benefited from Northeastern University's Advanced Scientific Computation Center (ASCC), theory support at the Advanced Light Source, Berkeley and the allocation of time at the NERSC supercomputing center through DOE grant number DE-AC02-05CH11231.

REFERENCES AND NOTES

1. Teo, J.; Fu, L.; Kane, C. Surface States and Topological Invariants in Three-Dimensional Topological Insulators: Application to Bi_{1-x}Sb_x. *Phys. Rev. B* **2008**, *78*, 045426.
2. Kane, C. L.; Mele, E. J. Z₂ Topological Order and the Quantum Spin Hall Effect. *Phys. Rev. Lett.* **2005**, *95*, 146802.
3. Hsieh, D.; Qian, D.; Wray, L.; Xia, Y.; Hor, Y. S.; Cava, R. J.; Hasan, M. Z. A Topological Dirac Insulator in a Quantum Spin Hall Phase. *Nature* **2008**, *452*, 970–974.
4. Fu, L.; Kane, C.; Mele, E. Topological Insulators in Three Dimensions. *Phys. Rev. Lett.* **2007**, *98*, 106803.
5. Hasan, M. Z.; Kane, C. L. Colloquium: Topological Insulators. *Rev. Mod. Phys.* **2010**, *82*, 3045–3067.
6. Zhang, H.; Liu, C.-X.; Qi, X.-L.; Dai, X.; Fang, Z.; Zhang, S.-C. Topological Insulators in Bi₂Se₃, Bi₂Te₃, and Sb₂Te₃ with a Single Dirac Cone on the Surface. *Nat. Phys.* **2009**, *5*, 438–442.
7. Cha, J. J.; Williams, J. R.; Kong, D.; Meister, S.; Peng, H.; Bestwick, A. J.; Gallagher, P.; Goldhaber-Gordon, D.; Cui, Y. Magnetic Doping and Kondo Effect in Bi₂Se₃ Nanoribbons. *Nano Lett.* **2010**, *10*, 1076–1081.
8. Hatch, R. C.; Bianchi, M.; Guan, D.; Bao, S.; Mi, J.; Iversen, B. B.; Nilsson, L.; Hornekaer, L.; Hofmann, P. Stability of the Bi₂Se₃(111) Topological State: Electron-Phonon and Electron-Defect Scattering. *Phys. Rev. B* **2011**, *83*, 241303.
9. Schubert, G.; Fehske, H.; Fritz, L.; Vojta, M. Fate of Topological-Insulator Surface States Under Strong Disorder. *Phys. Rev. B* **2012**, *85*, 201105.
10. Read, N.; Green, D. Paired States of Fermions in Two Dimensions with Breaking of Parity and Time-Reversal Symmetries and the Fractional Quantum Hall Effect. *Phys. Rev. B* **2000**, *61*, 10267–10297.
11. Kato, Y. K.; Myers, R. C.; Gossard, A. C.; Awschalom, D. D. Observation of the Spin Hall Effect in Semiconductors. *Science* **2004**, *306*, 1910–1913.
12. Wunderlich, J.; Kaestner, B.; Sinova, J.; Jungwirth, T. Experimental Observation of the Spin-Hall Effect in a Two-Dimensional Spin-Orbit Coupled Semiconductor System. *Phys. Rev. Lett.* **2005**, *94*, 047204.

13. König, M.; Wiedmann, S.; Brüne, C.; Roth, A.; Buhmann, H.; Molenkamp, L. W.; Qi, X.-L.; Zhang, S.-C. Quantum Spin Hall Insulator State in HgTe Quantum Wells. *Science* **2007**, *318*, 766–770.
14. Fu, L.; Kane, C. Superconducting Proximity Effect and Majorana Fermions at the Surface of a Topological Insulator. *Phys. Rev. Lett.* **2008**, *100*, 096407.
15. Qi, X.-L.; Li, R.; Zang, J.; Zhang, S.-C. Inducing a Magnetic Monopole with Topological Surface States. *Science* **2009**, *323*, 1184–1187.
16. Fu, L.; Kane, C. Josephson Current and Noise at a Superconductor/Quantum-Spin-Hall-Insulator/Superconductor Junction. *Phys. Rev. B* **2009**, *79*, 161408.
17. Xia, Y.; Qian, D.; Hsieh, D.; Wray, L.; Pal, A.; Lin, H.; Bansil, A.; Grauer, D.; Hor, Y. S.; Cava, R. J.; Hasan, M. Z. Observation of a Large-Gap Topological-Insulator Class with a Single Dirac Cone on the Surface. *Nat. Phys.* **2009**, *5*, 398–402.
18. Zhang, T.; Cheng, P.; Chen, X.; Jia, J.-F.; Ma, X.; He, K.; Wang, L.; Zhang, H.; Dai, X.; Fang, Z.; Xie, X.; Xue, Q.-K. Experimental Demonstration of Topological Surface States Protected by Time-Reversal Symmetry. *Phys. Rev. Lett.* **2009**, *103*, 1–4.
19. Checkelsky, J. G.; Hor, Y. S.; Cava, R. J.; Ong, N. P. Bulk Band Gap and Surface State Conduction Observed in Voltage-Tuned Crystals of the Topological Insulator Bi_2Se_3 . *Phys. Rev. Lett.* **2011**, *106*, 196801.
20. Zhang, Y.; He, K.; Chang, C.-Z.; Song, C.-L.; Wang, L.-L.; Chen, X.; Jia, J.-F.; Fang, Z.; Dai, X.; Shan, W.-Y.; et al. Crossover of the Three-Dimensional Topological Insulator Bi_2Se_3 to the Two-Dimensional Limit. *Nat. Phys.* **2010**, *6*, 584–588.
21. Sakamoto, Y.; Hirahara, T.; Miyazaki, H.; Kimura, S.-I.; Hasegawa, S. Spectroscopic Evidence of a Topological Quantum Phase Transition in Ultrathin Bi_2Se_3 films. *Phys. Rev. B* **2010**, *81*, 165432.
22. Kong, D.; Randal, J. C.; Peng, H.; Cha, J. J.; Meister, S.; Lai, K.; Chen, Y.; Shen, Z.-X.; Manoharan, H. C.; Cui, Y. Topological Insulator Nanowires and Nanoribbons. *Nano Lett.* **2010**, *10*, 329–333.
23. Cho, S.; Butch, N. P.; Paglione, J.; Fuhrer, M. S. Insulating Behavior in Ultrathin Bismuth Selenide Field Effect Transistors. *Nano Lett.* **2011**, *11*, 1925–1927.
24. Hong, S. S.; Kundhikanjana, W.; Cha, J. J.; Lai, K.; Kong, D.; Meister, S.; Kelly, M. A.; Shen, Z.-X.; Cui, Y. Ultra-Thin Topological Insulator Bi_2Se_3 Nanoribbons Exfoliated by Atomic Force Microscopy. *Nano Lett.* **2010**, *10*, 3118–3122.
25. Zhao, S. Y. F.; Beekman, C.; Sandilands, L. J.; Bashucky, J. E. J.; Kwok, D.; Lee, N.; LaForge, A. D.; Cheong, S. W.; Burch, K. S. Fabrication and Characterization of Topological Insulator Bi_2Se_3 Nanocrystals. *Appl. Phys. Lett.* **2011**, *98*, 141911.
26. Kong, D.; Dang, W.; Cha, J. J.; Li, H.; Meister, S.; Peng, H.; Liu, Z.; Cui, Y. Few-Layer Nanoplates of Bi_2Se_3 and Bi_2Te_3 with Highly Tunable Chemical Potential. *Nano Lett.* **2010**, *10*, 2245–2250.
27. Peng, H.; Lai, K.; Kong, D.; Meister, S.; Chen, Y.; Qi, X.-L.; Zhang, S.-C.; Shen, Z.-X.; Cui, Y. Aharonov-Bohm Interference in Topological Insulator Nanoribbons. *Nat. Mater.* **2010**, *9*, 5.
28. He, L.; Xiu, F.; Yu, X.; Teague, M.; Jiang, W.; Fan, Y.; Kou, X.; Lang, M.; Wang, Y.; Huang, G.; Yeh, N.-C.; Wang, K. L. Surface-Dominated Conduction in a 6 nm Thick Bi_2Se_3 Thin Film. *Nano Lett.* **2012**, *12*, 1486–1490.
29. Bansal, N.; Kim, Y. S.; Edrey, E.; Brahl, M.; Horibe, Y.; Iida, K.; Tanimura, M.; Li, G.-H.; Feng, T.; Lee, H.-D.; et al. Epitaxial Growth of Topological Insulator Bi_2Se_3 Film on Si(111) with Atomically Sharp Interface. *Thin Solid Films* **2011**, *520*, 20.
30. Kim, Y. S.; Brahl, M.; Bansal, N.; Edrey, E.; Kapilevich, G. A.; Iida, K.; Tanimura, M.; Horibe, Y.; Cheong, S.-W.; Oh, S. Thickness-Dependent Bulk Properties and Weak Antilocalization Effect in Topological Insulator Bi_2Se_3 . *Phys. Rev. B* **2011**, *84*, 073109.
31. Bianchi, M.; Hatch, R. C.; Mi, J.; Iversen, B. B.; Hofmann, P. Simultaneous Quantization of Bulk Conduction and Valence States through Adsorption of Nonmagnetic Impurities on Bi_2Se_3 . *Phys. Rev. Lett.* **2011**, *107*, 086802.
32. King, P.; Hatch, R.; Bianchi, M.; Ovsyannikov, R.; Lupulescu, C.; Landolt, G.; Slomski, B.; Dil, J.; Guan, D.; Mi, J. L.; et al. Large Tunable Rashba Spin Splitting of a Two-Dimensional Electron Gas in Bi_2Se_3 . *Phys. Rev. Lett.* **2011**, *107*, 096802.
33. Zhang, J.; Peng, Z.; Soni, A.; Zhao, Y.; Xiong, Y.; Peng, B.; Wang, J.; Dresselhaus, M. S.; Xiong, Q. Raman Spectroscopy of Few-Quintuple Layer Topological Insulator Bi_2Se_3 Nanoplatelets. *Nano Lett.* **2011**, *11*, 2407–2414.
34. Min, Y.; Moon, G. D.; Kim, B. S.; Lim, B.; Kim, J.-S.; Kang, C.-Y.; Jeong, U. Quick, Controlled Synthesis of Ultrathin Bi_2Se_3 Nanodiscs and Nanosheets. *J. Am. Chem. Soc.* **2012**, *134*, 2872–2875.
35. Wang, D.; Yu, D.; Mo, M.; Liu, X.; Qian, Y. Preparation and Characterization of Wire-Like Sb_2Se_3 and Flake-Like Bi_2Se_3 Nanocrystals. *J. Cryst. Growth* **2003**, *253*, 445–451.
36. Linder, J.; Yokoyama, T.; Sudbø, A. Anomalous Finite Size Effects on Surface States in the Topological Insulator Bi_2Se_3 . *Phys. Rev. B* **2009**, *80*, 1–5.
37. Lu, H.-Z.; Shan, W.-Y.; Yao, W.; Niu, Q.; Shen, S.-Q. Massive Dirac Fermions and Spin Physics in an Ultrathin Film of Topological Insulator. *Phys. Rev. B* **2009**, *81*, 7.
38. Gajdoš, M.; Hummer, K.; Kresse, G.; Furthmüller, J.; Bechstedt, F. Linear Optical Properties in the Projector-Augmented Wave Methodology. *Phys. Rev. B* **2006**, *73*, 045112.
39. Perdew, J. P.; Burke, K.; Ernzerhof, M. Generalized Gradient Approximation Made Simple. *Phys. Rev. Lett.* **1996**, *77*, 3865–3868.
40. Blöchl, P. E. Projector Augmented-Wave Method. *Phys. Rev. B* **1994**, *50*, 17953–17979.
41. Kresse, G.; Joubert, D. From Ultrasoft Pseudopotentials to the Projector Augmented-Wave Method. *Phys. Rev. B* **1999**, *59*, 1758–1775.
42. Kresse, G.; Hafner, J. *Ab Initio* Molecular Dynamics for Open-Shell Transition Metals. *Phys. Rev. B* **1993**, *48*, 13115–13118.
43. Kresse, G.; Furthmüller, J. Efficiency of *ab Initio* Total Energy Calculations for Metals and Semiconductors Using a Plane-Wave Basis Set. *Comput. Mater. Sci.* **1996**, *6*, 15–50.
44. Kresse, G.; Furthmüller, J. Efficient Iterative Schemes for *ab Initio* Total-Energy Calculations Using a Plane-Wave Basis Set. *Phys. Rev. B* **1996**, *54*, 11169–11186.
45. Tanemura, S.; Miao, L.; Kajino, Y.; Itano, Y.; Tanemura, M.; Toh, S.; Kaneko, K.; Mori, Y. Fabrication and Optical Characterization of Vanadium Oxide Nano-Particulates Thin Film. *J. Mater. Sci.: Mater. Electron.* **2007**, *18*, 43–46.
46. Yazyev, O. V.; Kioupakis, E.; Moore, J. E.; Louie, S. G. Quasiparticle Effects in the Bulk and Surface-State Bands of Bi_2Se_3 and Bi_2Te_3 Topological Insulators. *Phys. Rev. B* **2012**, *85*, 161101.
47. Hsieh, T. H.; Fu, L. Majorana Fermions and Exotic Surface Andreev Bound States in Topological Superconductors: Application to $\text{Cu}_x\text{Bi}_2\text{Se}_3$. *Phys. Rev. Lett.* **2012**, *108*, 107005.
48. Kane, R. S.; Cohen, R. E.; Silbey, R. Theoretical Study of the Electronic Structure of PbS Nanoclusters. *J. Phys. Chem.* **1996**, *100*, 7928–7932.
49. Ellingson, R. J.; Beard, M. C.; Johnson, J. C.; Yu, P.; Micic, O. I.; Nozik, A. J.; Shabaev, A.; Efros, A. L. Highly Efficient Multiple Exciton Generation in Colloidal PbSe and PbS Quantum Dots. *Nano Lett.* **2005**, *5*, 865–871.
50. Konstantatos, G.; Clifford, J.; Levina, L.; Sargent, E. H. Sensitive Solution-Processed Visible-Wavelength Photodetectors. *Nat. Photonics* **2007**, *1*, 531–534.
51. Kim, J. I.; Kim, J.; Lee, J.; Jung, D.-R.; Kim, H.; Choi, H.; Lee, S.; Byun, S.; Kang, S.; Park, B. Photoluminescence Enhancement in CdS Quantum Dots by Thermal Annealing. *Nano-scale Res. Lett.* **2012**, *7*, 482.
52. McIver, J. W.; Hsieh, D.; Steinberg, H.; Jarillo-Herrero, P.; Gedik, N. Control Over Topological Insulator Photocurrents with Light Polarization. *Nat. Nanotechnol.* **2012**, *7*, 96–100.